Macromolecular Bioscience
www.mbs-journal.de

Investigating How All-Trans Retinoic Acid Polycaprolactone (atRA-PCL) Microparticles Alter the Material Properties of 3D Printed Fibrin Constructs

Maria V. Hangad, Alejandro Forigua, Kali Scheck, Stephanie M. Willerth, and Katherine S. Elvira**

The 3D printing of human tissue constructs requires carefully designed bioinks to support the growth and function of cells. Here it is shown that an additional parameter is how drug-releasing microparticles affect the material properties of the scaffold. A microfluidic platform is used to create all-trans retinoic acid (atRA) polycaprolactone (PCL) microparticles with a high encapsulation efficiency (85.9 ± 5.0%), and incorporate them into fibrin constructs to investigate their effect on the material properties. An encapsulation that is around 25–35% higher than the current state of the art batch methods is achieved. It is also found that the drug loading concentration affects the microparticle size, which can be controlled using the microfluidic platform. It is shown that the release of atRA is slower in fibrin constructs than in buffer, and that the presence of atRA in the microparticles modulates both the degradation and the rheological properties of the constructs. Finally, it is shown that the fibrin material exhibits a stronger solid-like state in the presence of atRA-PCL microparticles. These findings establish a basis for understanding the interplay between drug-releasing microparticles and scaffold materials, paving the way for bioinks that achieve tailored degradation and mechanical properties, together with sustained drug delivery for tissue engineering applications.

1. Introduction

3D bioprinting is a manufacturing technique that uses digital designs to create 3D structures by depositing successive layers of biomaterials, cells and growth factors. The aim is to fabricate functional tissues for use in regenerative medicine and tissue engineering.[1,2] The use of 3D printing provides more control over the shape of the construct. Achieving optimal structures with 3D bioprinting involves the use of smart bioinks, which are specially formulated to recreate the native cellular environment. These bioinks incorporate bioactive molecules, cells, and responsive elements such as drug delivery systems to enhance cell viability, proliferation, and differentiation, thereby improving the functionality of the 3D printed constructs.[2,3]

A variety of biomaterials—natural, synthetic, metallic, and ceramic—have been explored for the formulation of 3D printed constructs.[4] In the field of neural tissue engineering, natural materials such as fibrin,

M. V. Hangad, A. Forigua[+], K. S. Elvira
Department of Chemistry
University of Victoria
Victoria, BC V8W 2Y2, Canada
E-mail: kelvira@uvic.ca

M. V. Hangad, A. Forigua[+], S. M. Willerth, K. S. Elvira
Centre for Advanced Materials and Related Technology (CAMTEC)
University of Victoria
Victoria, BC V8W 2Y2, Canada
E-mail: willerth@uvic.ca

K. Scheck, S. M. Willerth
Division of Medical Sciences
University of Victoria
Victoria, BC V8W 2Y2, Canada

S. M. Willerth
Department of Mechanical Engineering
University of Victoria
Victoria, BC V8W 2Y2, Canada

S. M. Willerth
Department of Biomedical Engineering
University of Victoria
Victoria, BC V8W 2Y2, Canada

S. M. Willerth
School of Biomedical Engineering
University of British Columbia
Vancouver, BC V6T 1Z3, Canada

The ORCID identification number(s) for the author(s) of this article can be found under https://doi.org/10.1002/mabi.202400464

[+]Present address: Department of Chemical Engineering, McGill University, Montréal, QC H3A 0C5, Canada

[The copyright line for this article was changed on 26 March 2025 after original online publication.]

DOI: 10.1002/mabi.202400464

alginate, and chitosan have gathered particular interest due to their unique properties and compatibility with neural cells. Fibrin, known for its biocompatibility and biodegradability, supports stem cell culture and differentiation.[5–7] This protein-based material serves as an excellent foundation for neural tissue scaffolds. Building upon this foundation, alginate, an anionic polysaccharide, can be incorporated to enhance the structural integrity of 3D printed constructs. Alginate is ionically cross-linked in bioinks through divalent ions such as calcium (Ca^{2+}), resulting in stable viscoelasticity, stiffness, and rapid gelation time.[8–11] Like fibrin, alginate has also been shown to promote the growth of neural stem cells in vitro.[12]

To further improve the mechanical properties of these scaffolds, chitosan, a cationic polysaccharide, can be added to the bioink formulation. The interaction of chitosan with alginate in the presence of calcium ions (Ca^{2+}) leads to increased storage and loss moduli, as well as improved tensile strength. This enhancement is attributed to the ionic interactions with alginate and the covalent bonding facilitated by genipin, which together improve the structural integrity of the scaffold and its suitability for biological applications.[13–15] Components such as fibrin, alginate, and chitosan, when integrated into fibrin-based scaffolds, offer a compatible 3D architecture that mimics the extracellular matrix, promoting cell differentiation and proliferation while closely resembling in vivo tissue environments.[16] To further enhance the functionality of these scaffolds, drug delivery systems can also be incorporated into the bioink formulation.

Drug delivery systems such as microparticles offer precise and targeted administration of active agents to achieve specific therapeutic outcomes, and can also be used for cell differentiation.[17,18] Microparticles range in size between 1 and 1,000 µm, and can encapsulate drugs, proteins, or other bioactive agents.[19] In the field of 3D printing, microparticles serve multiple functions such as providing controlled release of therapeutic agents, enhancing cell adhesion and proliferation, and modulating the mechanical properties of the 3D printed constructs.[20] Recent studies highlight the potential of 3D printing to create multi-functional scaffolds with integrated drug delivery systems and tailored mechanical properties.[21–23] However, many of these approaches rely heavily on post-printing modifications or are limited by a lack of control over drug release profiles and scaffold degradation dynamics during fabrication, with only a few studies exploring the integration of microparticles within the bioink during the printing process to achieve simultaneous control over mechanical properties and drug release.[24,25]

One such application of drug-releasing microparticles is their incorporation into fibrin-based bioinks for cell culture scaffolding. By incorporating microparticles within fibrin-based bioinks, researchers can better mimic in vivo conditions while also tailoring the release kinetics of bioactive agents.[26,27] However, the material properties of printed fibrin scaffolds containing drug-releasing microparticles have not been thoroughly characterized.[28] This characterization is important, as the intrinsic and extrinsic material properties within the scaffold can significantly change cell–cell interactions, along with their ability to build their own extracellular matrix and sustain their function as living tissues while the biomaterial-based scaffold degrades.

Understanding the interactions between drugs, drug-releasing microparticles, and the scaffolding materials used in bioinks is crucial when designing smart bioinks that enable the creation of biomimetic or humanized artificial tissues. These interactions can significantly affect the mechanical properties of the scaffold and the behavior of the therapeutics within the 3D printed construct.[29] Therefore, a study that considers both the structural and pharmacological aspects of smart bioinks is essential for advancing the field of tissue engineering and developing more effective 3D printed tissues.

Polycaprolactone (PCL) is commonly used as a polymeric material for the design of smart bioinks that include drug delivery particles due to its biocompatibility, biodegradability under biological conditions, and slow release profile.[30,31] Previous studies have demonstrated the effectiveness of PCL as a carrier and delivery vehicle for various molecules for stem cell differentiation into neurons, including all-trans retinoic acid (atRA),[32,33] guggulsterone,[34] and purmorphamine.[35] In addition to delivering cargo and aiding in cell differentiation, thereby reducing the need for frequent media changes, PCL has been shown to improve the mechanical properties (elastic modulus) of 3D printed constructs by approximately 30%.[36] While their size, dispersity, and drug loading are determined solely during the microparticle fabrication process, the effects that the bioink has on the drug release profile of PCL microparticles, as well as the effect of the microparticles on the degradation of the 3D scaffold itself, remain unexplored. Understanding these effects is crucial for optimizing the design and functionality of bioinks, thereby avoiding cell death or unwanted phenotype expression during cell culture in a 3D printed scaffold.

Various methods are used for the fabrication of PCL microparticles, including batch and semi-batch methods,[19,37] as well as microfluidic methods.[38] Notable benefits of using microfluidic platforms for microparticle fabrication, compared to traditional batch and semibatch methods, include cost-effectiveness and the control they provide over droplet size and distribution, leading to enhanced manufacturing processes.[39,40] Traditional batch production of PCL microparticles, typically involving the creation of oil-in-water emulsions followed by precipitation of the microparticles and solvent evaporation, lacks the precision offered by microfluidic technologies, particularly regarding control over the particle size. Microfluidic methods also provide increased control over the encapsulation of water-insoluble drugs within a polymer matrix.[41,42] By using the enhanced control provided by microfluidic platforms to create microparticles of precise size and loading, the properties of smart bioinks used for tissue engineering can be further optimized.

Here we investigate the impact that atRA-PCL microparticles have on the material properties of 3D printed fibrin constructs. We use a microfluidic platform to create a range of microparticles with bespoke characteristics to study the effect of microparticle formulation parameters on their size, encapsulation efficiency, and drug loading capacity. We find that use of our microfluidic platform allows us to achieve an around 25–35% higher encapsulation of atRA in PCL microparticles when compared to non-microfluidic methods. We then show that atRA release is modulated by the fibrin scaffold environment, with slower release observed in constructs compared to buffer. We also quantify the effect of the microparticles on the mechanical properties of fibrin constructs, showing that they cause a faster degradation of the constructs, while increasing their solid-like state.

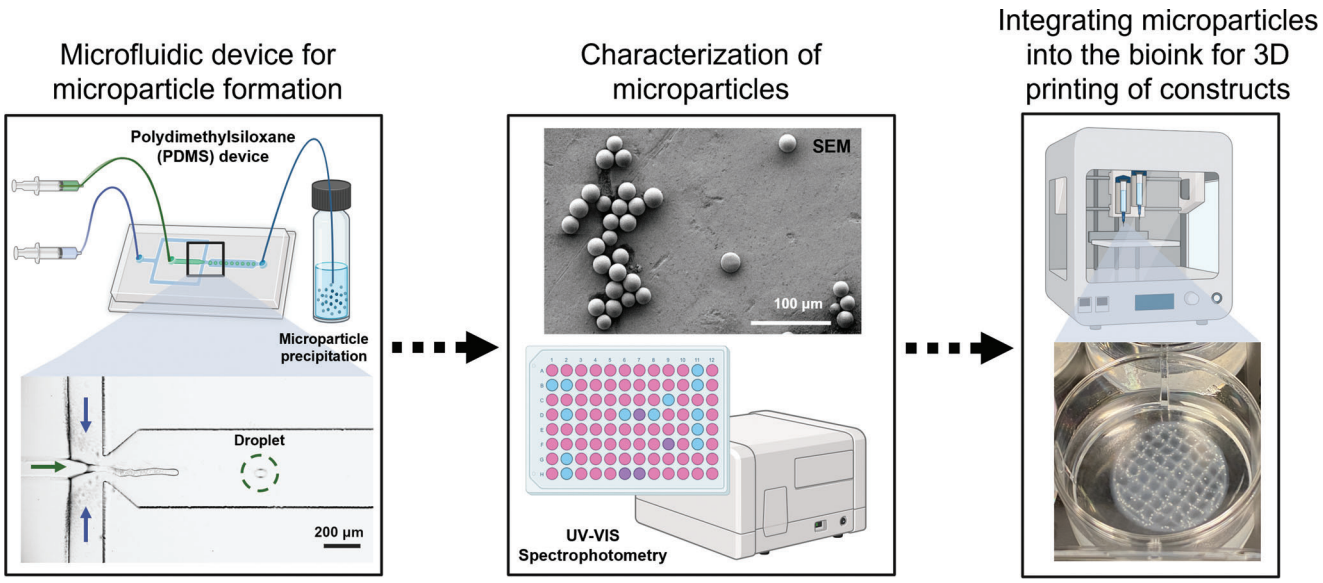

Figure 1. Overview of the experimental workflow for the creation and characterisation of atRA-PCL microparticles in 3D printed fibrin constructs. Microparticle fabrication from oil-in-water droplets on a microfluidic device was followed by microparticle characterization using SEM and UV–Vis spectrophotometry. Microparticles with the highest encapsulation efficiency were then seeded into fibrin constructs to investigate their release kinetics. Figures without scale bars were created in BioRender.

This work establishes proof-of-concept principles for integrating drug-releasing microparticles into fibrin-based bioinks, focusing on material compatibility, controlled release profiles, mechanical properties and degradation dynamics, with the broader aim of advancing localized drug delivery systems for sustained therapeutic release in tissue engineering applications.

2. Experimental Section

2.1. Materials

Polydimethylsiloxane (PDMS, Dow Sylgard 184) was purchased from Ellsworth Adhesives. Polyvinyl alcohol (PVA, MW 13 000–23 000, 87–89% hydrolyzed), polycaprolactone (PCL, MW 70 000–90 000), all-trans retinoic acid (atRA, >98%), chlorotrimethylsilane (>98%), dimethyl sulfoxide (DMSO, >99%), glacial acetic acid (>99%), tris buffered saline (TBS, pH 7.6), phosphate buffered saline (PBS, pH 7.4), calcium chloride, thrombin, chitosan, genipin and β-glycerolphosphate (β-GP) were purchased from Sigma–Aldrich. Dichoromethane (DCM, >99.8%) was purchased from VWR International. Ethanol (>95%) and isopropanol (>95%) were purchased from Commercial Alcohols. Polytetrafluoroethylene tubing (PTFE, 1/16 inch outer diameter, 750 µm inner diameter) was purchased from Chromatographic Specialities. Fibrinogen was purchased from EMD Milipore. A 5% (w/v) high-viscosity alginate solution was purchased prepackaged from Cellink, containing sodium alginate (MW 120 000–190 000), D-mannitol and HEPES buffer. Agarose (Froggarose-LE) was purchased from FroggaBio. 3 mL pneumatic cartridges (SKU: CSC010311101) and 22-gauge needles (SKU: NZ6220505001) for the BIO X 3D-bioprinter (Gen. 3) were purchased from Cellink.

2.2. Overview of the Experimental Workflow

As shown in **Figure 1**, a PDMS microfluidic device was designed to enable the formation of microparticles with a range of sizes and drug loading concentrations. Oil-in-water droplets were created at a flow-focusing junction on the microfluidic device and collected off-chip in a glass vial to allow microparticle precipitation. Then, both the droplets and the microparticles were characterised. The droplet volume was calculated from images taken on-chip and the microparticles were characterised off-chip using scanning electron microscopy (SEM) to assess their size and morphology, and ultraviolet–visible (UV–Vis) spectrophotometry to quantify encapsulation efficiency. The microparticles were then incorporated into fibrin-based bioinks that were used for the 3D printing of fibrin constructs. The release kinetics of the microparticles within the fibrin constructs were measured, and compared to the release kinetics of the microparticles in buffer. Finally, rheological measurements of the fibrin constructs were performed to quantify differences in material properties based on the presence of microparticles in the bioink.

2.3. Preparation of Solutions for Microparticle Formation

The aqueous phase (2% w/v PVA) was prepared by dissolving 4 g of PVA in 200 mL of deionized water and mixing at 85 °C and 850 rpm until a clear solution was formed. The oil phase was prepared by dissolving 800 mg of PCL into 15 mL of DCM and mixing at 900 rpm until a clear solution was formed. To form drug-loaded microparticles, the oil phase was dosed with increasing amounts of atRA stock (0.04 M in DMSO) to form 6 µg RA/mg PCL, 10 µg RA/mg PCL and 25 µg RA/mg PCL solutions.

2.4. Fabrication of the Microfluidic Devices

The microfluidic devices were fabricated as described previously.[38] In brief, the PDMS microfluidic devices were fabricated by soft lithography. For this, the master mould (silicon wafer) was placed in a desiccator with 50 µL of chlorotrimethylsilane for 45 min. The wafer was then clamped in a 3D printed holder, followed by pouring a PDMS mix (10:1 w/w, base to curing agent) on top of the mould. After degassing the PDMS for 60 min, it was left to cure overnight at 65 °C. The cured PDMS was peeled from the mould, cut into individual devices, and inlet and outlet holes were punched with a 1 mm biopsy punch. Glass microscope slides were used as the device substrates. The devices and microscope slides were thoroughly cleaned with a sequential cycle of soapy Milli-Q water, Milli-Q water, isopropanol and ethanol. They were dried by blowing with filtered air, and baking at 90 °C for 30 min. The clean devices and microscope slides were treated with air plasma (Diener Electronic, Zepto ONE, 60 s, 100 W, 0.60 mbar). Activated surfaces were brought into contact following the plasma treatment, bonding the PDMS device to the glass microscope slide.

The microfluidic channel surfaces were immediately treated after bonding. For this, 2% w/v PVA (same as above) was loaded into a 1 mL Hamilton glass gas-tight syringe. The syringe was attached to a piece of PTFE tubing and connected to one inlet of the device, with a second piece of tubing connected to the outlet. All other inlets or outlets in the device were plugged using small pieces of sealed tubing. The PVA solution was manually pushed through the device for 10 min, filling the device channels. This was followed by blowing filtered air through the device to remove excess PVA. The devices were baked at 100 °C for 15 min and kept at 65 °C for at least 72 h before use.

2.5. Microparticle Production on the Microfluidic Device

The methods for particle production have been adapted from our previous work.[38] In brief, droplet formation was performed on a microfluidic device mounted on a Nikon Eclipse Ti2-U inverted microscope, paired with a Phantom VEO 710L high-speed camera for imaging. The oil and aqueous phases were flowed through the device using neMESYS syringe pumps (Cetoni, Germany) with 1 and 25 mL Hamilton syringes attached to the device via PTFE tubing. For stable droplet formation, flow rates were gradually increased until a 300 to 1 µL min^{-1} ratio of aqueous to oil flow rates was reached. The flow rate ratio was then adjusted to a final flow rate of 350 to 0.5 µL min^{-1} for droplet collection. For droplet collection, the PTFE tubing connected to the device outlet was placed into a 10 mL glass vial filled with 2 mL of PVA solution (same as above). The vial containing the sample was then capped, manually inverted for 30 s and left at room temperature overnight in the dark to allow for extraction of DCM and microparticle precipitation.

The formed microparticles were recovered by removing the excess PVA solution from the sample vial and then transferring the leftover solution into 1.5 mL Eppendorf tubes. Once transferred, the microparticles were washed with Milli-Q water and centrifuged at 7,000 rpm for 7 min, followed by 5 subsequent washes with Milli-Q water at 5,000 rpm for 5 min. After the last wash, the sample was freeze-dried in a lyophilizer (VirTis Freezemobile 12EL –85 °C FreezeDryer Lyophilizer w/16-Port Tree Manifold) for 24 h. The samples were stored at –80 °C until used.

2.6. Size Measurements of Droplets and Microparticles

Droplet Morphometry and Velocimetry (DMV) video processing software was used to measure on-chip droplet sizes as they formed.[43] In brief, the software processed each frame by subtracting the background from the original image. By increasing the contrast of the image, the software detected the edge of the droplets, which allowed it to calculate the droplet diameter. DMV uses the device channel width to set a scale for measurements.

Microparticles were imaged and measured off-chip using SEM (Hitachi 2-4800) following protocols from our previous work.[36,38] The prepared microparticles were loaded onto an SEM stub using 50 µL of ethanol for even distribution. The microparticles were then sputter-coated with gold-palladium (Anatech Hummer VI, Au/Pd) with plasma discharge at a current of 10 mA for 4 min before imaging. The microparticle diameters were measured using the Quartz-PCL Image Management Systems software (Quartz Systems).

2.7. Quantification of Encapsulation Efficiency

The encapsulation of cargo (atRA) in the microparticles at increasing loading concentrations was quantified using UV–Vis spectrophotometry (SpectraMax M5 plate reader) at 354 nm by breaking open the particles. Before measurement, the microparticles were placed in a 1.5 mL Eppendorf tube, re-dissolved into 300 µL of DCM and vortexed at 350 rpm for 5 min. Then, 1 mL of 95% ethanol was added, followed by vortexing at 15 000 rpm for 5 min. The solution was then cooled to –80 °C for 5 min before centrifuging at 15 000 rpm for 5 min to fully precipitate the PCL from the supernatant solution. This protocol created a clear supernatant solution containing the intended drug (atRA) with an opaque precipitate at the bottom of the tube. The supernatant was removed from the Eppendorf tube and loaded into the plate reader for analysis. The reported absorbance values are triplicate measurements of three different batches of microparticles produced on three different microfluidic devices. A standard curve was used to determine the concentration of atRA in the samples (see the Supporting Information). The encapsulation efficiency (%E.E.) is calculated as a ratio of the atRA detected once the microparticles are broken open (the cargo) divided by the initial concentration of atRA in each polymer solution (the loading concentration), as follows:

$$\%\text{E.E.} = \left(\frac{[\text{atRA}]\text{measured}}{[\text{atRA}]o}\right) \cdot 100\% \quad (1)$$

2.8. Preparation of Fibrin-Based Bioink and Crosslinker

The fibrin-based bioink and crosslinker were prepared as described previously.[8,44] In brief, a fibrinogen stock (50 mg mL^{-1}) was formed by dissolving fibrinogen in TBS. A genipin stock solution (25 mg mL^{-1}) was prepared by reconstituting solid genipin

in DMSO. This solution facilitates the covalent crosslinking of chitosan to fibrin. The bioink was prepared by mixing the solutions with sodium alginate such that the final concentration in the bioink was: 20 mg mL^{-1} fibrinogen, 0.3 mg mL^{-1} genipin and 1% w/v sodium alginate. Microparticles were re-suspended in TBS for a final concentration of 1 mg mL^{-1} in bioink.

Similarly, the crosslinker was prepared by mixing to a concentration of 20 mg mL^{-1} calcium chloride and 1.7 UM mL^{-1} thrombin, both dissolved in TBS. Thrombin is an enzyme that cleaves fibrinogen into fibrin monomers, playing a crucial role in the fibrin polymerization process. Chitosan was prepared by dissolving 25 mg of chitosan into 1% v/v acetic acid and sterilized in an autoclave for 30 min. The pH of the crosslinker was adjusted to 7.4 using β-GP so that the final concentration of the chitosan in the crosslinker was 0.075% w/v.

2.9. 3D Printing Fibrin Constructs

3D printing was conducted as previously described.[44] To summarize, 3D printing was performed using a BioX 3D printer. The support bath for the printed fibrin constructs consisted of a 0.5% w/v agarose solution prepared by mixing agarose at 1 000 rpm until fully dissolved, autoclaving it at 121 °C, and cooling it to room temperature to form a slurry due to the high concentration used. For in vitro drug release studies, 10 × 3 mm cylinders with 20 layers and 25% infill were printed, consistent with previous fibrin-based bioink studies seeded with drug-releasing microparticles.[44,45] For rheological measurements, 25 × 2 mm cylinders with five layers were printed to maintain consistency with our previous work.[36] Along with the dimensions, the gap size and sample height were kept consistent,[36] with all constructs printed using the same number of layers and bioink volume. Minor variability due to pneumatic printing pressure fluctuations was minimized by maintaining uniform layer numbers and operating conditions across all samples.

To print the fibrin constructs, the bioink was transferred to a 5 mL plastic syringe attached to a female-to-female luer lock connector and a 3 mL pneumatic cartridge. A 22-gauge printing needle was attached to the cartridge. For all prints, the pressure was set to 11 mm s^{-1} and the speed to 15 kPa, allowing the needle tip to shear through the agarose and lay high-resolution fibers while maintaining fiber thickness. The fibrin constructs were printed into 3 mL agarose support baths in a 6-well plate. After printing, crosslinker was injected around the construct perimeter using a 10 mL syringe with a 22-gauge needle. Constructs were left at room temperature for 30 min to crosslink, then transferred to a dish of TBS to remove excess agarose and stored in PBS at 4 °C. Crosslinking conditions, including time and method, followed established protocols to ensure reproducibility and consistent fibrin scaffold formation.[36,37,44] Fully crosslinked constructs retained their shape during handling and rheometry, ensuring consistency across all samples.

2.10. In Vitro Release Kinetics

The release kinetics of atRA both from the microparticles and from fibrin constructs seeded with microparticles, were measured by UV–Vis spectrophotometry at 354 nm on a SpectraMax M5 plate reader reader, following our previous protocol.[37] Control constructs containing unloaded microparticles (no atRA) were prepared under identical conditions to account for potential absorbance contributions from scaffold components. The measurements were obtained in triplicate from three different batches of microparticles and fibrin constructs. The standard curve used for quantification is available in the Supporting Information.

For the microparticles, release studies were performed by suspending atRA-loaded microparticles in PBS, centrifuging at 5,000 rpm for 5 min to form the supernatant solution, and re-suspending the pellet in 1 mL of fresh PBS. The suspension/extraction cycle was done every 2 days for 14 days. The supernatant solution was inserted into the plate reader for measurement and quantification of the atRA released from the microparticles. After the supernatant extraction and measurement on day 14, the remaining suspension was processed (the particles were broken open) as outlined above to quantify the atRA remaining unreleased during the 14-day period.

To measure atRA release from microparticles in the fibrin constructs, a 3D printed 10 × 3 mm cylinder with 20 layers and 25% grid infill was used. The fibrin construct was removed from the agarose bath, submerged in a 6-well plate filled with 1 mL of PBS and placed in a non-sterile incubator at 37 °C. To measure the atRA released into the PBS, 1 mL of PBS was extracted from each sample well for measurement every two days for 12 days. 1 mL of fresh PBS was then added to re-suspend the fibrin constructs in each sample well to account for the PBS removed. In addition, the mass of each cylindrical fibrin construct was measured using an analytical balance every 2 days for 12 days to monitor the degradation of the fibrin constructs.

2.11. Rheological Analysis of Fibrin Constructs

Clear fibrin constructs with no microparticles (control), fibrin constructs with microparticles (no cargo) and fibrin constructs with microparticles (with cargo) were examined to quantify their viscoelastic and mechanical properties. For this, rheological analysis was performed on the fibrin constructs using an Anton Paar Rheometer with a 25 mm sandblasted parallel plate geometry (PP25/S). The frequency sweeps were from 0.1 to 100 rad s^{-1} with a strain of 0.5%. Viscosity curves were created using shear rates from 0.01 to 100 Hz.

Fibrin constructs were printed in a disc-shape design with dimensions of 25 x 2 mm and left overnight in a 4 °C incubator. The fibrin constructs were loaded onto the stage and were trimmed to match the geometry of the rheometer. The parallel plate was lowered with a 1 mm gap between the stage so that the fibrin construct was pressed between the geometry and the stage during each test. All measurements were performed in triplicate for three different 3D printed cylinders.

2.12. Statistical Analysis

The data for the effect of drug loading on droplet/microparticle sizes was analyzed using a one-way ANOVA, and a Tukey's post hoc analysis was used to assess the significance of each drug

loading group compared to each other. The same statistical tests were used for the release kinetics. All statistical analyses were performed at a confidence level of 95% ($p < 0.05$).

3. Results and Discussion

3.1. Drug Loading Concentration Affects Microparticle Size

To investigate how the microparticle cargo affects release kinetics and microparticle mechanical properties upon incorporation into bioinks for 3D printing, we first developed a suite of microparticles with different cargo concentrations. The use of microfluidic devices enables us to create microparticles in a tunable, predictable, and controlled manner. The experimental workflow involves the creation of the microparticles using the microfluidic device, characterization of the resulting microparticles, and the integration and evaluation of the effects of the loaded microparticles on fibrin constructs (Figure 1). A flow-focusing microfluidic device developed in-house was used for the fabrication of atRA-loaded PCL microparticles.[38] Our previous research demonstrated that the inclusion of cargo directly impacts droplet and microparticle sizes.[38] Therefore, it was of particular interest to investigate how the initial loading concentration of atRA ($[atRA]_o$) influences microparticle size and encapsulation efficiency (%E.E.). The $[atRA]_o$ is the concentration of atRA added to the microfluidic device to form the microparticles, with the encapsulation efficiency (%E. E.) determining how much of that becomes incorporated into the microparticles.

The flow-focusing geometry and the hydrophilic nature of the microfluidic channels achieved droplet generation in a jetting regime, resulting in the formation of oil-in-water (o/w) droplets, as illustrated in Figure 1. Stable droplet formation was attained at oil and aqueous flow rates of 350 and 0.5 µL min^{-1}, respectively. The droplets were collected in a vial and stored overnight, showing no evidence of droplet merging (i.e., coalescence) as they precipitated to form solid microparticles. **Figure 2** shows the size distribution of droplets (on the microfluidic device), and the size distribution and the SEM images of the microparticles (after precipitation) produced over a range of $[atRA]_o$ (w/w, atRA/PCL) as follows: no cargo (Figure 2A,B), 6 µg mg^{-1} (Figure 2C,D), 10 µg/mg (Figure 2E,F), and 25 µg mg^{-1} (Figure 2G,H). By changing the amount of atRA in the oil phase, the effect on droplet and microparticle size could be observed.

Figure 2 shows that the addition of atRA correlates with a decrease in both droplet and microparticle sizes ($p < 0.05$). Although this phenomenon has not been explored for atRA-PCL microparticles, a similar effect has been observed in previous studies with PCL microparticles containing other cargos created on a microfluidic device.[46,47] This effect can be attributed to alterations in fluid phases, which impact droplet generation phenomena.[38,48] Although these prior studies have explored the overarching effects of cargo incorporation, an exploration into the impact of increasing quantities of cargo provides insights to aid in the design of custom-made microparticles tailored for targeted applications (3D printing in this case). By systematically increasing the $[atRA]_o$, we can observe the effects of this variable on the sizes of the fabricated microparticles.

The addition of cargo causes a reduction in the microparticle size which plateaus once a loading concentration of 10 µg mg^{-1} is reached. Significant changes ($p < 0.05$) in mean microparticle sizes were observed between the 0 µg mg^{-1} to 6 µg mg^{-1} samples and between the 6 µg mg^{-1} and 10 µg mg^{-1} samples, resulting in a decrease in both droplet and microparticle sizes. However, the final increment in cargo to 25 µg mg^{-1} showed no quantifiable change in droplet or microparticle size in comparison to the other tested concentrations (6 µg mg^{-1} vs 25 µg mg^{-1} and 10 µg mg^{-1} vs 25 µg mg^{-1}). Table 1 summarizes the range of droplet and microparticle sizes obtained for each $[atRA]_o$. From these observations we can infer a limiting effect on the decrease in droplet/microparticle size at drug loading concentrations above an optimal threshold. Future work could investigate how this optimal drug loading concentration may vary using different cargos or polymers when fabricating microparticles using microfluidic devices.

3.2. Microfluidic Device Enables High Efficiency Encapsulation of atRA-PCL in Microparticles

We are able to achieve a high level of encapsulation (85.9 ± 5.0%) of atRA into PCL microparticles, with current batch methods achieving an encapsulation efficiency (%E. E.) in the range of only 50–60%.[32,49] **Table 2** shows the encapsulation efficiency of atRA in the microparticles created on our microfluidic device for each initial drug loading concentration ($[atRA]_o$). The maximum encapsulation efficiency (85.9 ± 5.0%) is achieved at a $[atRA]_o$ of 10 µg mg^{-1} (w/w, atRA/PCL). Statistical analysis (one-way ANOVA and Tukey's post hoc analysis) shows significant differences ($p < 0.05$) in the %E.E. when comparing the microparticles initially loaded with 10 µg mg^{-1} cargo to those initially loaded with 6 µg mg^{-1} or 25 µg mg^{-1} cargo (6 µg mg^{-1} and 25 µg mg^{-1} are the same).

We hypothesize that the higher encapsulation achieved at an $[atRA]_o$ of 10 µg mg^{-1} is likely is due to the solvent interactions that occur involving DCM and DMSO as the droplets harden into PCL microparticles via solvent evaporation. These solvent interactions are enabled by the rapid mixing and high surface-area-to-volume ratios of droplets within the microfluidic device, promoting uniform distribution of the drug within the droplets and reducing the formation of empty carriers.[50] Evidence from literature suggests that the water-miscible properties of DMSO allow for its immediate diffusion from the dispersed to the continuous phase, leading to faster solvent evaporation and higher encapsulation.[51,52] Furthermore, microfluidic-based polymer microparticle fabrication has shown increased effectiveness in the encapsulation of lipid-soluble drugs compared to those made in batch, offering a controlled and reproducible environment which decreases the risk of drug loss and aggregation, leading to improved encapsulation.[41,42]

3.3. Drug Release is Mediated by Microparticles in Scaffold Constructs

To understand the drug release behaviour of our bespoke microparticles under cell-like environments, the release kinetics of particles with the highest %E.E. (microparticles with a $[atRA]_o$ of 10 µg mg^{-1}) were quantified before and after integration in the

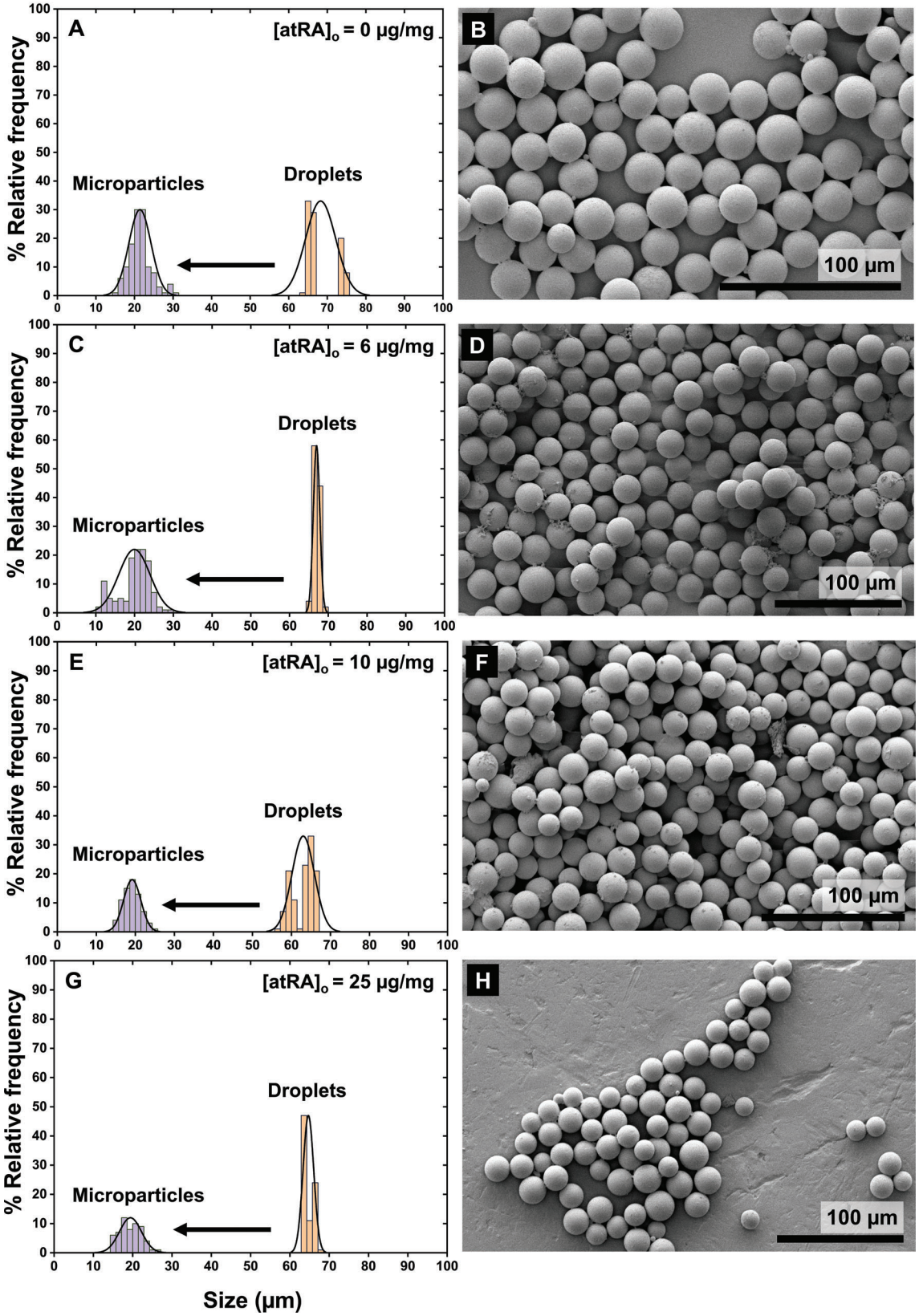

Figure 2. Comparison of the on-chip droplet size (yellow data) with the off-chip microparticle size (purple data) with increasing $[atRA]_o$ in the oil phase. Histograms (left column) display the % relative frequency counts of droplets or microparticles versus size. The number of bins is 70 for each histogram. The plotted curve on each histogram represents the fitted normal distribution. The initial drug loading concentration ($[atRA]_o$) in each case is: A) and

Table 1. Summary of average droplet (on-chip) and microparticle (off-chip) sizes generated for each initial drug loading concentration ([atRA]$_o$, μg mg^{-1}, w/w, atRA/PCL). These data are shown graphically in Figure 2. STD is the standard deviation and %CV* is the coefficient of variation, a measure of the size of the distribution.

(μg mg^{-1}) [atRA]$_o$	Droplet size (μm)	STD	% CV*	Microparticle size (μm)	STD	%CV*
0	68.4	4.0	5.8	21.4	2.7	12.5
6	67.0	0.8	1.2	20.2	3.9	19.2
10	63.1	2.8	4.5	19.1	1.8	9.6
25	64.2	1.1	1.8	19.6	2.2	11.1

Table 2. Summary of encapsulation efficiency (% E.E) for each intial drug loading concentration of atRA/PCL (μg/mg, w/w). $N = 3$ for each drug loading concentration.

[atRA]$_o$ (μg mg^{-1})	%E.E.	STD	% CV
6	64.1	4.58	7.14
10	85.9	5.03	5.85
25	62.2	7.25	11.7

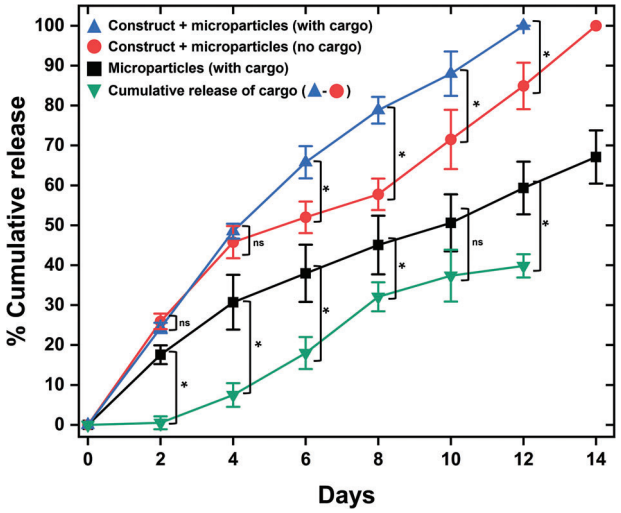

Figure 3. Drug release behavior of atRA microparticles and scaffold-mediated effects on release kinetics. The microparticles had a 10 μg mg^{-1} drug loading concentration and were produced at a flow rate ratio of 350:0.5 μL min^{-1} (oil/aqueous) on our microfluidic platform. Black squares represent the cumulative release of atRA from PCL microparticles suspended in PBS over a 14-day period. Blue triangles indicate the total release from fibrin constructs seeded with atRA-loaded microparticles, while red circles correspond to constructs with unloaded microparticles (no drug cargo). Green triangles show the normalized cumulative release of atRA, obtained by subtracting the contributions of unloaded microparticles. This normalization isolates the release profile of atRA alone. The fibrin constructs degraded fully by day 12, while PCL microparticles in PBS continued releasing atRA until day 14. The concentration of drug released into the supernatant was determined using a standard curve (see the Supporting Information). $N = 3$ in each case, the error bars show the standard deviation, and statistical significance is shown with a star ($p < 0.05$, ns = non significant).

printed fibrin constructs, with additional controls used to account for non-cargo contribution. Sampling was performed every two days for a 14-day period. The data were normalized to isolate the release profile of atRA from other potential confounding factors.

Figure 3 compares the release kinetics of microparticles suspended in PBS buffer (black squares), constructs with microparticles containing atRA (blue triangles), constructs with unloaded microparticles (red circles), and the cumulative release of atRA alone (green triangles). By subtracting the background contributions of unloaded microparticles, the cumulative release of atRA alone (green triangles in Figure 3) was determined. This normalization process ensured that the signal measured corresponded solely to atRA release.

The release profile for the microparticles in buffer (black squares) showed a cumulative release of 67 ± 6.7% at the end of the 14 day period. There is a significant ($p < 0.05$) release of drug occurring from day 2, with an overall faster drug release when compared to other work using atRA-PCL microparticles.[32] The mechanism for drug release shown for the microparticles in buffer in Figure 3 aligns with literature by following zero-order kinetics likely due to a combination of surface erosion and ester hydrolysis of the PCL polymer.[53,54] Statistical analysis via a one-way ANOVA reveals significant differences in mean cumulative release of atRA from the PCL microparticles from day 4 onwards as part of the initial burst release that occurs on day 2. Although the trend in cumulative release as seen in the release profiles is typical for PCL, the slope of the curves (or the rate of percent atRA cumulative release) is faster. From this we can infer that a faster rate of degradation of the drug loaded PCL microparticles may be occurring than is typically seen in the literature. This may be due to the use of a higher molecular weight PCL (70 000–90 000 MW). Prior work has shown that lower degrees of crystallinity resulting from the use of higher molecular weight PCL can influence the rates of degradation.[55,56]

In contrast, the cumulative release of atRA in fibrin constructs was notably lower, achieving only 39 ± 2.9% by day 12 (green triangles). This indicates that the scaffold environment plays a critical role in modulating release behavior. The presence of the fibrin-alginate-chitosan matrix introduces several mechanisms that contribute to the slower release. Physically, the scaffold network acts as a diffusion barrier, limiting the free mobility of atRA. Chemically, electrostatic interactions between the negatively charged atRA and positively charged components of the scaffold, such as chitosan and calcium ions (Ca^{2+}), further restrict drug mobility. [57,58]

Additionally, the hydrophilic nature of the fibrin construct may influence both the degradation of the PCL microparticles and the release of atRA. The swelling behavior of fibrin constructs

B) no cargo, C) and D) 6 μg mg^{-1} (w/w, atRA/PCL), E) and F) 10 μg mg^{-1} (w/w, atRA/PCL) and G) and H) 25 μg mg^{-1} (w/w, atRA/PCL). $N = 150$ over an average of three runs for each data set at a flow rate of 350:0.5 μL min^{-1} (oil/aqueous). Sizes of droplets were measured on-chip using the Droplet Morphometry and Velocimetry software and microparticles were measured off-chip after solvent extraction using SEM for each drug loading concentration (right column). $N = 150$ over three runs for each data set obtained for the microparticle measurements using SEM. **Table 1** shows the average size, standard deviation, and coefficient of variation for each data set.

upon hydration creates a microenvironment that stabilizes hydrophobic molecules like atRA, reducing the overall release rate. Interestingly, this effect highlights a potential advantage of using composite hydrogels to achieve more controlled release kinetics. While the specific contributions of these ionic and physical interactions remain to be fully elucidated, these findings underscore the capacity of the scaffold to regulate drug delivery profiles effectively.[59–61]

The normalized cumulative release profile (green triangles) further emphasizes the impact of these scaffold-mediated interactions. While the constructs showed an initial burst release similar to microparticles in buffer (black squares), the overall trend was more gradual, suggesting that the scaffold matrix plays a significant role in extending release. From days 2 to 8, statistical analysis revealed significant differences ($p < 0.05$) in release profiles between the two conditions. By day 12, the fibrin constructs had fully degraded. This controlled release behavior contrasts sharply with the less restrictive release observed in PBS, demonstrating the efficacy of the scaffold in modulating delivery.

Mechanistically, the observed release behavior reflects a dynamic interplay between the inherent degradation of the PCL microparticles, ionic interactions within the scaffold matrix, and swelling-induced stabilization of hydrophobic molecules like atRA. The zero-order release kinetics observed in buffer reflect the inherent degradation behavior of PCL microparticles. However, in the fibrin constructs, first-order kinetics dominate, as interactions within the matrix alter both the release dynamics and the degradation pathway of the microparticles.[58,62] These findings offer valuable insights into the design of composite scaffolds for drug delivery and smart bioinks for tissue engineering, particularly in applications requiring sustained and controlled release. Furthermore this study demonstrates, for the first time, the ability of a fibrin-alginate-chitosan scaffold to modulate the release of atRA-loaded PCL microparticles, providing a robust framework for designing bioinks tailored for long-term therapeutic applications.

3.4. Presence of atRA in PCL Microparticles Increases Degradation of Fibrin Constructs

Given the difference in the release profile of atRA from PCL microparticles when they were included in the fibrin construct, we further investigated how the degradation of the fibrin constructs occurs upon the addition of the microparticles. To do this, we monitored changes in the masses of fibrin constructs seeded with and without atRA microparticles to visualize their degradation over 14 days. **Figure 4** shows the fibrin construct mass decrease over time for fibrin constructs with no microparticles (grey squares), fibrin constructs with unloaded microparticles (red circles) and fibrin constructs with microparticles loaded with atRA (blue triangles, $[atRA]_o = 10\ \mu g\ mg^{-1}$).

The degradation profile observed for all three conditions showed that for the first 2 days there was no significant difference in the degradation of the fibrin construct (~25% mass loss in each case). Similarly, from day 2 to day 6, statistical analysis reveals no significant differences in mass between each experimental condition, though the overall rate of degradation decreases. This is especially significant for the case of the fibrin construct with drug

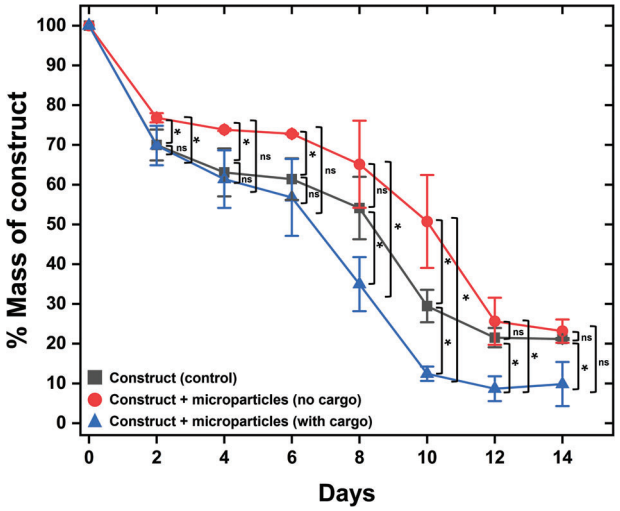

Figure 4. Effect of microparticles on the degradation of the fibrin construct over time. Fibrin construct mass loss shows the degradation of fibrin constructs over a 14 day period. Grey squares represent the control group of fibrin constructs with no microparticles. Red circles represent fibrin constructs seeded with microparticles with no drug cargo. Blue triangles represent fibrin constructs seeded with atRA microparticles ($[atRA]_o = 10\ \mu g\ mg^{-1}$). $N = 3$ in each case, using fibrin constructs with a 10 x 3 mm cylindrical design. Error bars show the standard deviation.

loaded microparticles, since the analysis showed an ~30% release of the cargo at this time. However, between day 8 and day 12, the mass loss between those releasing cargo (blue triangles) and the other two groups show a quantifiable difference. Microparticles with cargo caused a much faster mass loss in the fibrin construct, reaching close to 100% degradation at day 14.

Furthermore, from our prior analysis (Figure 3) we know that all the cargo has been released from the microparticles by day 12, implying that the presence of atRA in solution causes a faster degradation of the fibrin constructs than when the microparticles are present but have no cargo. This behavior is consistent with the literature, which shows that atRA, a negatively charged molecule, forms electrostatic complexes with cationic polymers like chitosan, potentially altering scaffold stability through ionic interactions.[58,59] Additionally, calcium ions (Ca^{2+}) are known to stabilize fibrin networks via specific binding sites on fibrinogen, and such interactions may be disrupted by atRA or other charged species within the scaffold environment [57]. Future work could explore these interactions in detail to better elucidate the role of specific bioink components in modulating scaffold stability, and to allow the creation of more bespoke bioink formulations.

It is important to note that the fibrin constructs seeded with microparticles with no cargo (red circles) show an overall slower degradation rate than the control fibrin construct which contained no microparticles at all (grey squares). This aligns with previous studies on similar fibrin constructs[36] and showcases how the PCL plays an advantageous role in maintaining the structural integrity of fibrin-based scaffolds. This highlights the importance of accounting for electrostatic interactions between the therapeutic, the crosslinker, and the scaffold material, which may influence degradation dynamics. Overall, our data suggest that the faster degradation of the fibrin constructs is primarily driven by interactions between the therapeutic (atRA) and the scaffold

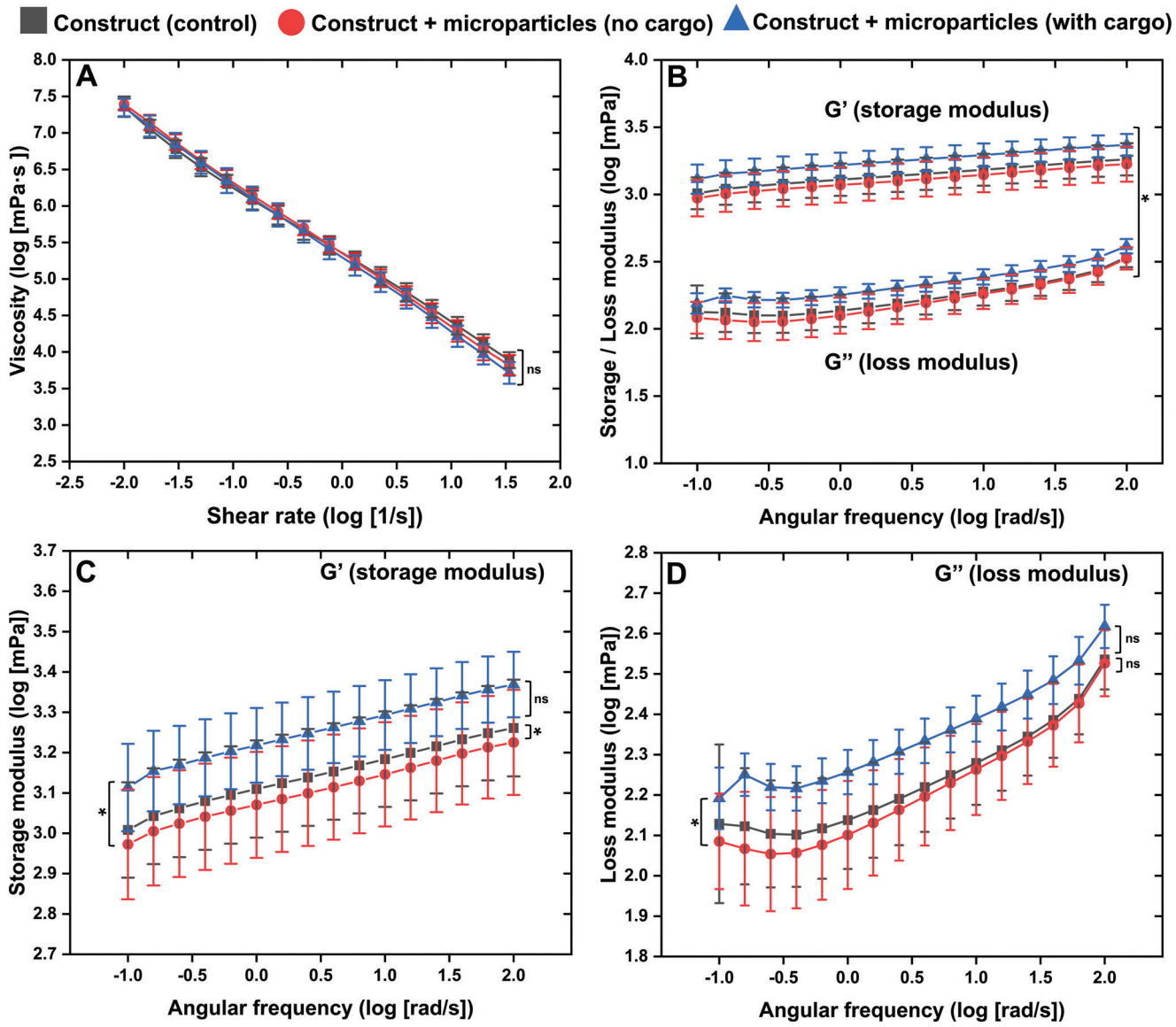

Figure 5. Effect of microparticles on the rheological properties of the 3D printed fibrin constructs. A) Change in viscosity over a range of shear rates, showing no significant differences (ns) across all groups. B) Change in storage modulus (G') and loss modulus (G'') over angular frequency, showing a significant difference ($p < 0.05$) between G' and G''. C) Expanded analysis of the storage modulus (G') across angular frequencies, highlighting significant differences ($p < 0.05$) between the formulations with and without cargo-loaded microparticles, as well as cargo loaded and control formulations. D) Expanded analysis of the loss modulus (G'') across angular frequencies, highlighting only significant differences ($p < 0.05$) between the formulations with and without cargo-loaded microparticles. C and D show the same data as B. Grey squares represent the control group of fibrin constructs with no microparticles. Red circles represent fibrin constructs seeded with microparticles without cargo. Blue triangles represent fibrin constructs seeded with microparticles with a $[atRA]_o$ of 10 µg mg^{-1}. $N = 3$ for each condition and error bars show the standard deviation.

components, including fibrin, calcium ions (Ca^{2+}), alginate, and chitosan, rather than by the presence of the PCL microparticles themselves.

3.5. Presence of atRA Promotes Stiffening of Fibrin Constructs

The mechanical properties of 3D printed fibrin constructs seeded with atRA-PCL microparticles were further assessed by investigating the viscosity of the material versus its shear rate, along with its storage modulus (G') and loss modulus (G''). Viscosity was measured at shear rates of 0.01 to 90 Hz to quantitatively investigate the deformation properties of the material. Determination of the storage and loss moduli was done by printing 25 x 2 mm disc-shaped fibrin constructs and applying a frequency sweep from 0.1 to 100 rad s^{-1} at a 0.5% strain.[36] In both cases, rheological data was acquired for fibrin constructs with no microparticles (grey squares), fibrin constructs with unloaded microparticles (red circles) and fibrin constructs with microparticles loaded with atRA (blue triangles, $[atRA]_o = 10$ µg mg^{-1}).

Figure 5A shows that the viscosity decreases at increasing shear rates across all tested, fully crosslinked constructs.

This consistent shear-thinning behavior aligns with prior studies,[63–65] as well as with our prior work,[36] showing flow behavior index values within the typical range of $0 < n < 1$. The composite bioink components, such as alginate and chitosan, contribute to this property, preserving extrudability and elasticity even after crosslinking.[36,64] These findings suggest that the addition of atRA-PCL microparticles does not significantly alter the viscoelastic properties of the fibrin constructs. Shear-thinning behaviour is ideal in bioinks as it enables them to flow or experience deformation more readily while retaining their elastic shape during the extrusion process, hence protecting living cells from the 3D printing extrusion process.[66]

Frequency sweeps (Figure 5B) show the G' and G'' properties of each experimental group as described above. These data are consistent with our previous published work.[36] Overall, a trend can be seen showing how G' is greater than G'' as angular frequency increases in all cases. This is confirmed through statistical analysis using a one-way ANOVA and post-hoc Tukey test, with G' and G'' being significantly different. A greater storage modulus compared to loss modulus demonstrates good elastic retention, allowing for the preservation of shape within the fibrin construct.

When comparing the G' of the fibrin constructs, there is a significant difference between population means of fibrin constructs with unloaded microparticles (red circles) and the control group consisting of fibrin constructs with no microparticles (grey squares). However, this difference is not seen when comparing the G'' values. This shows that the addition of PCL microparticles influences elastic retention during deformation more than viscous flow, effectively allowing fibrin constructs to behave more solid-like than liquid-like. Furthermore, the addition of the drug cargo to the PCL microparticles causes an increase in both the G' and G'' values of the fibrin constructs with angular frequency in a manner comparable to previous literature.[36]

Overall, these rheological data suggest that atRA microparticles do not affect the shear-thinning behavior of fibrin-based bioinks, but they significantly contribute to fibrin constructs becoming more solid-like. This is shown by the increase in storage modulus (G'), which indicates enhanced elastic retention and structural integrity under deformation. Increases in storage modulus for embedded particles in fibrin-alginate hydrogels has been shown before.[67] Such behavior is advantageous for scaffolds intended for load-bearing or mechanically dynamic environments, where maintaining shape stability is critical. The ability to tune the solid-like properties of fibrin constructs through the inclusion of drug-loaded microparticles highlights the potential for designing bioinks tailored for specific tissue engineering applications. For example, the interactions between scaffold components such as chitosan, fibrin, and the encapsulated therapeutic could be optimized to modulate cross-linking density and mechanical performance, providing a pathway for creating bespoke bioinks with controlled stiffness and elasticity.

Future studies could investigate how these microparticles influence the cross-linking within fibrin constructs and whether the observed stiffening behavior is linked to ionic interactions or specific polymer-drug interactions. Additionally, the assessment of mechanical properties at multiple time-points could provide a deeper understanding of the scaffold degradation. Understanding these mechanisms will enable the rational design of bioinks with tunable viscoelastic properties, enhancing their functionality in various biological environments and advancing their translation into clinical settings.

4. Conclusion

This study highlights the influence of drug-releasing microparticles on the material properties of 3D printed fibrin-based bioinks, with a focus on their potential for therapeutic delivery and tissue engineering applications. We demonstrate that atRA-loaded PCL microparticles can promote controlled degradation of fibrin constructs while maintaining desirable mechanical properties. Using a microfluidic platform, we achieved high encapsulation efficiency ($85.9 \pm 5.0\%$) and controlled microparticle size, representing a 25–35% improvement over traditional methods. Importantly, we found that atRA release is slower in fibrin constructs compared to buffer, highlighting the critical role of scaffold composition in modulating drug release profiles. Additionally, the presence of atRA promoted faster degradation of the fibrin constructs, underscoring the need to consider therapeutic-scaffold interactions during bioink design. Rheological analysis also confirmed that the addition of microparticles, with or without cargo, enhances the solid-like behavior of fibrin constructs without altering their shear-thinning properties. By providing a foundation for understanding the interactions between therapeutics, drug-releasing microparticles and scaffold materials, this work offers valuable design principles for creating bioinks with tailored release kinetics, material degradation and mechanical properties, and therapeutic functionality, enabling broader applications in tissue engineering.

Supporting Information

Supporting Information is available from the Wiley Online Library or from the author.

Acknowledgements

The authors acknowledge and respect the Lekwungen peoples on whose traditional territory the University of Victoria stands, and the Songhees, Esquimalt and WSÁNEĆ peoples whose historical relationships with the land continue to this day. K.S.E. was funded through the Canada Research Chair program and the Michael Smith Health Research B. C. Scholar program in partnership with the Canadians for Leading Edge Alzheimer Research Foundation. Her laboratory was equipped using funding from the Canada Foundation for Innovation John R. Evans Leaders Fund (CFI-JELF) and the British Columbia Knowledge Development Fund (BCKDF). A.F. was funded through her Natural Sciences and Engineering Research Council of Canada (NSERC) Discovery grant. S.M.W. received funding from the NSERC Discovery grant program, the Canadian Institutes of Health Research (CIHR) Project grant program, the NSERC CREATE program, Michael Smith Health Research B. C., the Pacific Parkinson's Research Institute, and the British Columbia Foundation for Non-Animal Research.

Conflict of Interest

Dr Willerth is co-founder and C.E.O. of Axolotl Biosciences, a biotechnology company that sells novel bioinks for 3D bioprinting.

Author Contributions

M.V.H. and A.F. contributed equally to this work. M.V.H. acquired all the experimental data. A.F. conceptualized the project. M.V.H. and A.F. performed the data and statistical analyses, made the figures and wrote the first draft. K.S. assisted with fibrin bioink and crosslinker production used for 3D printing for the rheological analysis, as well as for experiments with drug release in the fibrin constructs. K.S. wrote the first draft of the Experimental Section on 3D printing and rheological analysis of the fibrin constructs. M.V.H., A.F., and K.S.E. wrote the first version of the manuscript. S.M.W. revised the manuscript. A.F. and K.S.E. revised the final manuscript. S.M.W. and K.S.E. co-supervised M.V.H. S.M.W. supervised K.S. K.S.E. supervised A.F.

Data Availability Statement

The data that support the findings of this study are available from the corresponding author upon reasonable request.

Keywords

3D printing, all-trans retinoic acid, bioink, drug release, fibrin, microparticles, microfluidics, mechanical properties, polycaprolactone

Received: December 4, 2024
Published online: January 21, 2025

[1] S. V. Murphy, A. Atala, *Nat. Biotechnol.* **2014**, *32*, 773.
[2] M. J. Lerman, J. Lembong, G. Gillen, J. P. Fisher, *Appl. Phys. Rev.* **2018**, *5*, 4.
[3] I. Donderwinkel, J. C. Van Hest, N. R. Cameron, *Polym. Chem.* **2017**, *8*, 4451.
[4] A. Sachdev IV, S. Acharya, T. Gadodia, S. Shukla, J. Harshita, C. Akre, M. Khare, S. Huse, *Cureus* **2022**, *14*, 8.
[5] A. Shpichka, D. Osipova, Y. Efremov, P. Bikmulina, N. Kosheleva, M. Lipina, E. A. Bezrukov, R. B. Sukhanov, A. B. Solovieva, M. Vosough, P. Timashev, *Int. J. Bioprinting* **2020**, *6*, 3.
[6] M. Robinson, S. Douglas, S. M. Willerth, *Sci. Rep.* **2017**, *7*, 6250.
[7] J. M. Edgar, M. Robinson, S. M. Willerth, *Acta Biomater.* **2017**, *51*, 237.
[8] E. Abelseth, L. Abelseth, L. De La Vega, S. T. Beyer, S. J. Wadsworth, S. M. Willerth, *ACS Biomater. Sci. Eng.* **2019**, *5*, 234.
[9] K. Y. Lee, D. J. Mooney, *Prog. Polym. Sci.* **2012**, *37*, 106.
[10] C. C. Piras, D. K. Smith, *J. Mater. Chem. B* **2020**, *8*, 8171.
[11] F. E. Freeman, D. J. Kelly, *Sci. Rep.* **2017**, *7*, 17042.
[12] E. K. Purcell, A. Singh, D. R. Kipke, *Tissue Eng., Part C* **2009**, *15*, 541.
[13] P. Treenate, P. Monvisade, in *Macromolecular Symposia*, vol. *372*, Wiley Online Library, **2017**, pp. 147–153.
[14] Y. He, S. Derakhshanfar, W. Zhong, B. Li, F. Lu, M. Xing, X. Li, *J. Nanomater.* **2020**, *2020*, 2057097.
[15] M. Saberian, R. S. Roudsari, N. Haghshenas, A. Rousta, S. Alizadeh, *Heliyon* **2024**, *10*, e32040.
[16] L. De La Vega, D. A. Rosas Gómez, E. Abelseth, L. Abelseth, V. Allisson Da Silva, S. M. Willerth, *Appl. Sci.* **2018**, *8*, 2414.
[17] A. M. Bratt-Leal, R. L. Carpenedo, M. D. Ungrin, P. W. Zandstra, T. C. McDevitt, *Biomaterials* **2011**, *32*, 48.
[18] Z. Maan, N. Z. Masri, S. M. Willerth, *Biomolecules* **2022**, *12*, 141.
[19] A. Forigua, R. L. Kirsch, S. M. Willerth, K. S. Elvira, *J. Controlled Release* **2021**, *333*, 258.
[20] M. Sreepadmanabh, A. B. Arun, T. Bhattacharjee, *Biophys. Rev.* **2024**, *5*, 2.
[21] Y. Tan, S. Fan, X. Wu, M. Liu, T. Dai, C. Liu, S. Ni, J. Wang, X. Yuan, H. Zhao, Y. Weng, *Int. J. Biol. Macromol.* **2023**, *249*, 126028.
[22] C. Vyas, J. Zhang, Ø. Øvrebø, B. Huang, I. Roberts, M. Setty, B. Allardyce, H. Haugen, R. Rajkhowa, P. Bartolo, *Mater. Sci. Eng., C* **2021**,*118*, 111433.
[23] A. H. Yusop, M. N. Sarian, F. S. Januddi, Q. U. Ahmed, M. R. Kadir, D. Hartanto, H. Hermawan, H. Nur, *Mater. Des.* **2018**, *160*, 203.
[24] C. Bassand, F. Siepmann, L. Benabed, J. Verin, J. Freitag, S. Charlon, J. Soulestin, J. Siepmann, *J. Controlled Release* **2023**, *363*, 1.
[25] G. L. Koons, P. D. Kontoyiannis, L. Diaz-Gomez, S. Z. Elsarrag, D. W. Scott, M. Diba, A. G. Mikos, *3D Print. Addit. Manuf.* **2024**, *11*, e813.
[26] X. Shi, L. Cui, H. Sun, N. Jiang, L. Heng, X. Zhuang, Z. Gan, X. Chen, *Polym. Degrad. Stab.* **2019**, *161*, 319.
[27] Q. He, J. Zhang, Y. Liao, E. V. Alakpa, V. Bunpetch, J. Zhang, H. Ouyang, *Biotechnol. Adv.* **2020**, *39*, 107459.
[28] Q. Li, B. Chang, H. Dong, X. Liu, *Bioact. Mater.* **2023**, *25*, 485.
[29] M. P. Nikolova, M. S. Chavali, *Bioact. Mater.* **2019**, *4*, 271.
[30] A. Kumari, S. K. Yadav, S. C. Yadav, *Colloids Surf., B* **2010**, *75*, 1.
[31] N. Kamaly, B. Yameen, J. Wu, O. C. Farokhzad, *Chem. Rev.* **2016**, *116*, 2602.
[32] J. C. Gomez, J. M. Edgar, A. M. Agbay, E. Bibault, A. Montgomery, N. K. Mohtaram, S. M. Willerth, *Cell Mol. Bioeng.* **2015**, *8*, 307.
[33] L. De la Vega, L. Abelseth, R. Sharma, J. Trivino-Paredes, M. Restan, S. M. Willerth, *Adv. Nanobiomed Res.* **2021**, *1*, 2000077.
[34] A. Agbay, L. De La Vega, G. Nixon, S. Willerth, *Biomed. Mater.* **2018**, *13*, 034104.
[35] C. Benwood, J. Walters-Shumka, K. Scheck, S. M. Willerth, *Bioelectron. Med.* **2023**, *9*, 10.
[36] R. Sharma, R. Kirsch, K. P. Valente, M. R. Perez, S. M. Willerth, *Processes* **2021**, *9*, 1205.
[37] R. Sharma, C. Benwood, S. M. Willerth, *Curr. Protoc.* **2021**, *1*, e331.
[38] A. Forigua, A. Dalili, R. Kirsch, S. M. Willerth, K. S. Elvira, *ACS Appl. Polym. Mater* **2022**, *4*, 7004.
[39] B. Ferreira, P. Faria, J. Viegas, B. Sarmento, C. Martins, *Microfluidics in Pharmaceutical Sciences: Formulation, Drug Delivery, Screening, and Diagnostics* **2024**, 313.
[40] N. Convery, N. Gadegaard, *Micro and Nano Engineering* **2019**, *2*, 76.
[41] Q. Xu, M. Hashimoto, T. T. Dang, T. Hoare, D. S. Kohane, G. M. Whitesides, R. Langer, D. G. Anderson, *Small* **2009**, *5*, 1575.
[42] C. Busatto, J. Pesoa, I. Helbling, J. Luna, D. Estenoz, *Int. J. Pharm.* **2018**, *536*, 360.
[43] A. S. Basu, *Lab Chip* **2013**, *13*, 1892.
[44] J. Chrenek, R. Kirsch, K. Scheck, S. M. Willerth, *STAR Protocols* **2022**, *3*, 101348.
[45] I. Bilkic, D. Sotelo, S. Anujarerat, N. R. Ortiz, M. Alonzo, R. El Khoury, C. C. Loyola, B. Joddar, *Heliyon* **2022**, *8*, e12250.
[46] F. Heshmatnezhad, A. R. Solaimany Nazar, H. Aghaei, J. Varshosaz, *Soft Matter* **2021**, *17*, 10675.
[47] E. Rybak, P. Kowalczyk, S. Czarnocka-Śniadała, M. Wojasiński, J. Trzciński, T. Ciach, *Polymers* **2023**, *15*, 4375.
[48] E. E. Ekanem, S. A. Nabavi, G. T. Vladisavljević, S. Gu, *ACS Appl. Mater. Interfaces* **2015**, *7*, 23132.
[49] B. Mirani, E. Pagan, S. Shojaei, J. Duchscherer, B. D. Toyota, S. Ghavami, M. Akbari, *Eur. J. Pharmacol.* **2019**, *854*, 201.
[50] S. S. Aboelela, M. Ibrahim, A. Z. M. Badruddoza, V. Tran, J. K. Ferri, T. D. Roper, *Int. J. Pharm.* **2021**, *606*, 120906.
[51] N. V. N. Jyothi, P. M. Prasanna, S. N. Sakarkar, K. S. Prabha, P. S. Ramaiah, G. Y. Srawan, *J. Microencapsulation* **2010**, *27*, 187.
[52] J. Xu, S. Zhang, A. Machado, S. Lecommandoux, O. Sandre, F. Gu, A. Colin, *Sci. Rep.* **2017**, *7*, 4794.
[53] S. Fredenberg, M. Wahlgren, M. Reslow, A. Axelsson, *Int. J. Pharm.* **2011**, *415*, 34.
[54] P. Mandal, R. Shunmugam, *J. Macromol. Sci., Part A* **2021**, *58*, 111.

[55] M. J. Jenkins, K. L. Harrison, *Polym. Adv. Technol.* **2006**, *17*, 474.
[56] J.-C. Jeong, J. Lee, K. Cho, *J. Controlled Release* **2003**, *92*, 249.
[57] J. W. Weisel, R. I. Litvinov, *Blood, The J. Am. Soc. Hematology* **2013**, *121*, 1712.
[58] J. Maia, T. Santos, S. Aday, F. Agasse, L. Cortes, J. O. Malva, L. Bernardino, L. Ferreira, *ACS nano* **2011**, *5*, 97.
[59] C.-H. Han, T. S. Wiedmann, *Int. J. Pharm.* **1998**, *172*, 241.
[60] M. Bahadoran, A. Shamloo, Y. D. Nokoorani, *Sci. Rep.* **2020**, *10*, 7342.
[61] M. K. Younis, A. Z. Tareq, I. M. Kamal, *IOP Conf. Ser.: Mater. Sci. Eng.* **2018**, *454*, 012017.
[62] P. Paarakh, P. Ani Jose, S. CM, G. P. Christopher, *Int. J. Pharm. Res. Technol.* **2019**, *8*, 1.
[63] S. Freeman, R. Ramos, P. Alexis Chando, L. Zhou, K. Reeser, S. Jin, P. Soman, K. Ye, *Acta Biomater.* **2019**, *95*, 152.
[64] A. Cavallo, T. Al Kayal, A. Mero, A. Mezzetta, L. Guazzelli, G. Soldani, P. Losi, *J. Funct. Biomater.* **2023**, *14*, 459.
[65] R. V. Barrulas, M. C. Corvo, *Gels* **2023**, *9*, 986.
[66] A. Schwab, R. Levato, M. D'Este, S. Piluso, D. Eglin, J. Malda, *Chem. Rev.* **2020**, *120*, 11028.
[67] A. Richter, Y. Li, C. Rehbock, S. Barcikowski, A. Haverich, M. Wilhelmi, U. Böer, *Adv. Mater. Interfaces* **2021**, *8*, 2002015.